Materials Science & Engineering A 843 (2022) 143159

Contents lists available at ScienceDirect

Materials Science & Engineering A

journal homepage: www.elsevier.com/locate/msea

Microstructure and mechanical properties of V–Cr–Zr alloy with carbide and oxide strengthening

Ivan A. Ditenberg [a,b], Ivan V. Smirnov [a,b], Konstantin V. Grinyaev [a,b,*], Alexander N. Tyumentsev [a,b], Vyacheslav M. Chernov [c], Mikhail M. Potapenko [c]

[a] Institute of Strength Physics and Materials Science of the Siberian Branch of the Russian Academy of Sciences, Tomsk, 634055, Russia
[b] National Research Tomsk State University, Tomsk, 634050, Russia
[c] JSC Bochvar High-Technology Research Institute for Inorganic Materials, Moscow, 123098, Russia

ARTICLE INFO

Keywords:
Vanadium alloy
Thermomechanical treatment
Chemical-heat treatment
Microstructure
Mechanical properties
Dispersion strengthening

ABSTRACT

A comparative study of the effectiveness of carbide and oxide types of strengthening of V–Cr–Zr alloy was carried out by means of a comprehensive certification of structural-phase state parameters and measuring the mechanical properties characteristics. It has been shown that the use of chemical-heat treatment contributes to a significant increase in the thermal stability of the microstructure and mechanical properties of V–Cr–Zr alloy in comparison with carbide strengthening under the conditions of thermomechanical treatment. A controlled increase in the volume fraction of fine particles based on ZrO_2, along with an increase in the concentration of oxygen in the solid solution, leads to a decrease in the rate of oxides coagulation and an increase in the thermal stability of high disperse heterophase structure. These effects contribute to the retention of high defect structural states with nonzero values of crystal lattice curvature even after high-temperature (0.67 T_{melt}) anneals. The high efficiency of dispersion and substructural strengthening is a consequence of blocking dislocation slip by fine particles stabilized by oxygen in a solid solution.

1. Introduction

Among the main requirements for low-activation vanadium alloys as promising structural materials for thermonuclear power engineering is the provision of high-temperature strength while maintaining acceptable values of plasticity at low temperatures [1–5]. Due to the high chemical activity of such materials to interstitial impurities [6], they are characterized by the formation of corresponding solid solutions and the release of second phase particles.

One of the ways to improve the strength properties of vanadium alloys at high temperatures is to increase the efficiency of dispersion strengthening [7–14], due to dispersion, redistribution and increase in the volume fraction of fine second phase particles. For this purpose, various methods of thermomechanical (TMT) and chemical-heat (CHT) treatments are used. In this case, TMT methods predominantly contribute to an increase in the efficiency of the carbide type of strengthening by modifying the initial, vanadium-based metastable carbides and oxycarbonitrides into stable carbides based on diffusion-active substitution elements (Ti, Zr) [8,13]. In the case of CHT, the heterophase structure is modified by purposeful doping with interstitial elements (C, N, O), which is accompanied by both a change in the phase composition of second phase particles and an increase in their volume fraction. One of the effective methods of vanadium alloys CHT is internal oxidation (IO) [10,14,15], the use of which provides an increase in the concentration of oxygen and the formation of oxide particles. The latter, in turn, are characterized by high thermodynamic stability, which contributes to a significant (up to 0.8 T_{melt}) increase in the thermal stability of the alloy microstructure and mechanical properties.

Formation of structural-phase states with high effects of dispersion and substructural strengthening at high temperatures requires a uniform volume distribution of non-metallic phases fine particles, which, fixing high-defect structural states, suppress recrystallization processes [16]. Today, questions about the main factors that determine the efficiency of strengthening of heterophase alloys and the mechanisms of transformation of structural-phase states, depending on the processing conditions, are still relevant. Moreover, such studies are necessary for alloys

* Corresponding author. Institute of Strength Physics and Materials Science of the Siberian Branch of the Russian Academy of Sciences, Tomsk, 634055, Russia.
E-mail addresses: ditenbergia@ispms.tsc.ru (I.A. Ditenberg), smirnov_iv@ispms.tsc.ru (I.V. Smirnov), kvgrinyaev@ispms.tsc.ru (K.V. Grinyaev), tyuments@phys.tsu.ru (A.N. Tyumentsev), chernovv@bochvar.ru (V.M. Chernov), MMPotapenko@bochvar.ru (M.M. Potapenko).

https://doi.org/10.1016/j.msea.2022.143159
Received 9 January 2022; Received in revised form 12 April 2022; Accepted 14 April 2022
Available online 17 April 2022

with different elemental composition and volume fraction of fine particles, which is essential for optimizing the elemental composition of alloys and increasing the efficiency of the applied TMT and CHT methods.

In this work, a comparative study of the effect of carbide and oxide types of strengthening on structural-phase state parameters and mechanical properties characteristics, as well as their thermal stability, during thermomechanical and chemical-heat treatments of V–Cr–Zr alloy is carried out.

2. Materials and methods

We used vanadium alloy V–8.62Cr–0.66Zr–0.064O–0.036N–0.042C (at. %) (hereinafter V–Cr–Zr) obtained at JSC Bochvar High-Technology Research Institute for Inorganic Materials (Moscow, Russia). The combined treatment consisted of thermomechanical treatment according to regime II (TMT-II) [8,13] and chemical-heat treatment by the method of internal oxidation with the achievement of various oxygen concentrations [10,14].

TMT-II provides nanostructuring of the initial heterophase structure during the implementation of the mechanism of phase transformations by dissolving metastable vanadium carbides with subsequent segregation of the stable phase from the solid solution [8,13]. It includes 1-h annealing at T = 1400 °C and several (at least 3) cycles "rolling ε = (30–50) % at room temperature + annealing at T = (600–700) °C". Stabilizing vacuum annealing for 1 h was carried out at temperatures of 1000 or 1100 °C.

CHT was carried out on 1 mm-thick samples after TMT-II + 1100 °C and includes [10,14]: formation of surface scale during heat treatment in air at 600–700 °C, the duration of which is determined by the required oxygen concentration (C_O), vacuum (from 620 to 1000 °C) annealing for 9 h and stabilizing vacuum annealing at 1100 °C for 1 h.

The oxygen concentration after CHT was determined on the basis of data on the mass of samples before and after processing. The samples were weighted on electronic laboratory scales GH-200 (A&DCOLTD) with an accuracy of no worse than 10^{-4} g.

To study the thermal stability, the alloy samples after internal oxidation were annealed at 1200 °C ($0.67 \bullet T_{melt}$).

Electron BackScatter Difraction (EBSD [17]) patterns were obtained using a FEI Quanta 200 3D scanning electron-ion microscope with a Pegasus complex at accelerating voltage of 30 kV. Samples were prepared by mechanical grinding and subsequent electrolytic polishing in a 20 % solution of sulfuric acid in methanol at a voltage of 15 V. Orientation maps were obtained in the mode with hexagonal point setting. Kikuchi patterns formed by backscattered electrons were automatically indicated by the «TSL OIM data collection » software. Further processing of the resulting data was carried out using the «TSL OIM analysis » software.

Transmission electron microscopy studies were performed on Philips CM 30 TWIN (300 kV) and Philips CM 12 (120 kV) electron microscopes. Thin foils were obtained by jet electrolytic polishing on a MIKRON-3M device in a 20 % solution of sulfuric acid in methanol at a voltage of 15 V. The certification of high-defect structural states was carried out using the method of dark-field analysis of discrete and continuous misorientations [18], by studying the features of the behavior of extinction contours when the sample is tilted in a goniometer. Within the framework of the concept of bending-torsion tensor [19,20] (the tensor of the continuum dislocation density), this approach allows one to experimentally determine the quantitative values of some of the components of this tensor.

Mechanical tests of dog bone shaped specimens with the dimensions of the working section 13 mm × 2 mm × 1 mm were carried out by tension at a rate of $\dot{\varepsilon} = 2 \times 10^{-3}$ s^{-1} in vacuum of ≈2×10^{-5} Torr at temperatures of 20 °C, 800 °C and 900 °C.

Microhardness (HV) was determined by the prints of a Vickers diamond pyramid on a Neophot 21 instrument at a load of 0.5 N and a exposure time of 15 s.

3. Results

3.1. Microstructure

Fig. 1 represents the structural-phase state of V–Cr–Zr alloy after TMT-II with stabilizing annealing at 1000 °C. It was found that the grain structure, even after stabilization, is highly inhomogeneous. The grain orientation maps obtained by the EBSD method (Fig. 1a) show large anisotropic grains that are elongated in the rolling direction (RD) and reach a length of several hundred microns with a width ranging from 10 to 40 μm. The non-equiaxiality coefficient of such grains varies from 3 to 5. A strongly gradient color is observed inside such grains, which indicates the presence of structural states with low-angle misorientations of a discrete and/or continuous type. Against the background of large grains, there are both individual small grains and clusters of them. Their sizes in RD are from 5 to 15 μm, with a width from 5 to 10 μm. Non-equiaxiality coefficient of such grains does not exceed 3, and inside them, as a rule, there is no gradient color.

Fig. 1b shows a dark-field image obtained simultaneously in the [200] reflection from fine FCC ZrC particles and in the [110] reflection from the BCC vanadium matrix (Fig. 1c). It was found that after TMT-II, a high density of ZrC-based nanoparticles with sizes ranging from 2 to 20 nm is formed in the alloy. The lattice parameter of these particles (a) varies in the range 4.67–4.69 Å depending on the carbon concentration. Such particles, precipitating from the solid solution, form the Bain relationship with the matrix [21], in which the matrix reflection [110] BCC practically coincides with the [200] FCC from the particles of the second phases (Fig. 1c). Nanoparticles effectively fix the dislocation structure (Fig. 1b). Using the secant method [22], in the process of studying different sections of individual grains, it was found that the dislocation structure is not uniform. In some areas, the scalar dislocation density ($\rho_{\pm}$) does not exceed 10^9 cm^{-2}, while in others $\rho_{\pm}$ reaches 5×10^{10} cm^{-2}. Thus, fine-disperse ZrC-based particles formed as a result of TMT-II, fixing the dislocation structure, provide strengthening according to the Orowan mechanism [23]. According to this estimate, the maximum value of the volume fraction of ZrC-based second phase (f), based on the data on the chemical composition, reaches ≈ 0.08 %, which is limited by the low concentration of carbon in this alloy. In this case, the volume fraction of the entire oxycarbonitride phase of Zr(N, C, O) type based on Zr, as the most active phase-forming element, according to estimates, does not exceed 0.25 %.

Using transmission electron microscopy, by dark-field analysis of discrete and continuous misorientations, it has been established that crystal lattice curvature after TMT-II with stabilizing annealing at 1000 °C reaches 5 or more deg/μm. The presence of structural states characterized by a change in the crystal lattice orientation inside the grains is also evidenced by the gradient color of grain orientation maps obtained by EBSD method.

After TMT-II with stabilizing annealing at 1100 °C, against the background of large anisotropic grains elongated in RD, the formation of mostly medium-sized grains (20–40 μm) is observed, while small grains are rare (Fig. 2a). Note that coarse grains of anisotropic shape still retain the gradient color. Dark-field analysis of misorientations has shown that structural states with a crystal lattice curvature are rare, and its maximum values do not exceed 3 deg/μm. Intercrystalline boundaries of equiaxed grains of small and medium sizes, as well as low-angle boundaries of the fragments forming them, are often characterized by banded electron-microscopic contrast (Fig. 2b), which indicates their equilibrium state. In addition, a multiple decrease in the scalar dislocation density ($\rho_{\pm}$) was found in comparison with stabilization at 1000 °C. In the most defective areas it does not exceed 10^{10} cm^{-2} (Fig. 2c), while it is generally in the range from 5×10^8 cm^{-2} to 10^9 cm^{-2} (Fig. 2b). It is important to note that stabilizing annealing at 1100 °C does not affect the size and distribution of nanosized particles of

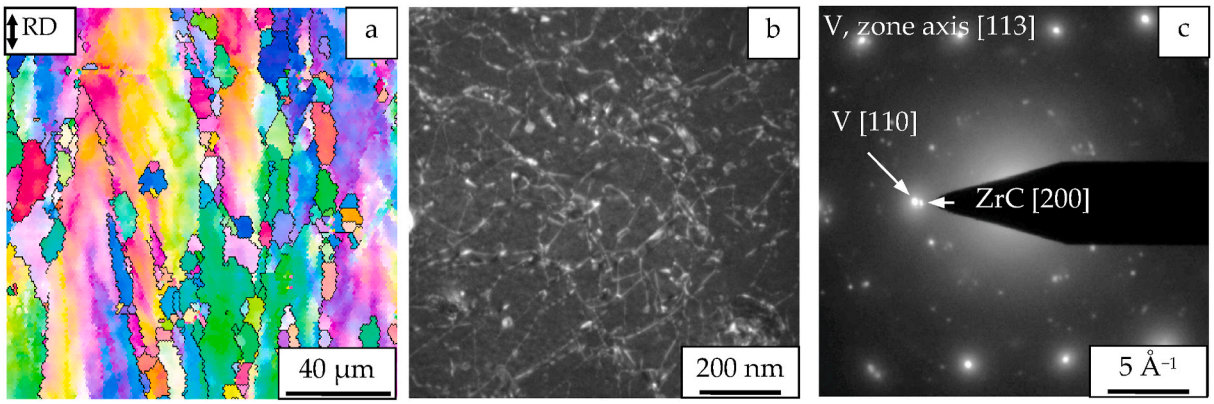

Fig. 1. Structural-phase state of V–Cr–Zr alloy after TMT-II with stabilizing annealing at 1000 °C. a – Grain orientation maps (SEM, EBSD). b – dark field image of fine-disperse ZrC-based carbides and pinned dislocations (TEM). c – microdiffraction pattern (TEM).

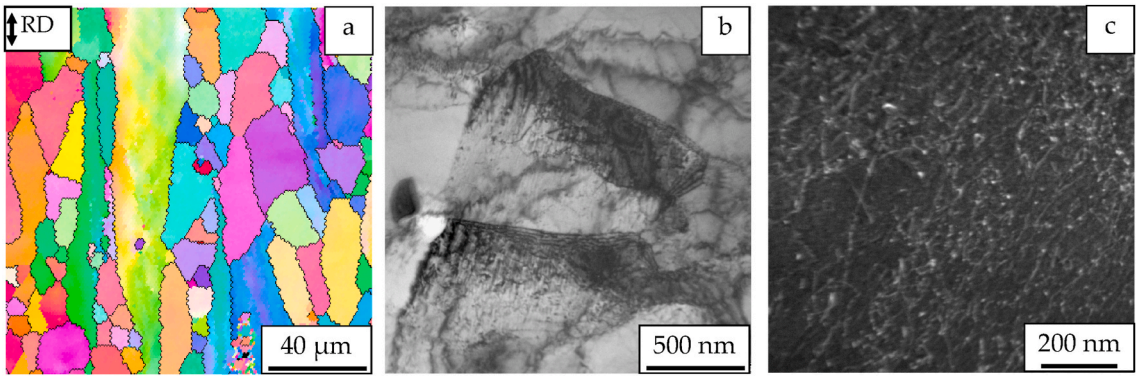

Fig. 2. Structural-phase state of V–Cr–Zr alloy after TMT-II with stabilizing annealing at 1100 °C. a – Grain orientation maps (EBSD). b – bright field microstructure image (TEM). c – dark field image of fine-disperse ZrC-based carbides and pinned dislocations (TEM).

the second phases (Fig. 2c).

Subsequent CHT with different durations of the stage of surface scale formation (oxidation in air) is characterized by the achievement of certain oxygen concentrations (C_O), the corresponding values of which, taking into account the initial oxygen concentration (0.064 at. %), are given in Table 1.

Fig. 3a shows a map of grain orientation of V–Cr–Zr alloy after CHT with an oxygen concentration of $C_O \approx 0.6$ at. % after stabilizing annealing at 1100 °C.

It was found that as a result of such treatment, a near-surface layer up to 80–100 μm thick is formed to the depth of oxygen penetration (oxidation front). The structure of this layer is presented by alternating coarse grains of an anisotropic shape, elongated in the rolling direction (RD), and interlayers of fine grains of a less elongated shape. Coarse grains reach a length of up to 100 μm with a width of no more than 30 μm and are characterized by a gradient color. Small grains with a gradient-free color reach 5–35 μm in length and 3–10 μm in width. At a distance of more than 100 μm from the surface, alternation of large anisotropic grains with interlayers of fine grains is also observed. In this case, coarse grains are characterized by a gradient color; their size, as after TMT, reaches several hundred μm in length, and their width ranges from 10 to 40 μm. Small grains with a gradient-free color are elongated in length (in RD) up to 50 μm with a width of 10–20 μm. Thus, after CHT with an oxygen concentration of $C_O \approx 0.6$ at. %, a near-surface layer is formed, the grain structure of which is smaller than the bulk of the material.

After reaching $C_O \approx 1$ at. % the oxygen penetration depth, and therefore the oxidation front, extends up to 250–280 μm from the sample surface (Fig. 3b). An increase in the oxygen concentration to $C_O \approx 1.3$ at. % ensures the realization of internal oxidation in the entire volume of the material, which on grain structure orientation maps manifests itself in the propagation of the oxidation front to a depth commensurate with the half-thickness of the sample (Fig. 3c).

It was established by transmission electron microscopy that after CHT and stabilizing annealing at 1100 °C, the oxidation front is characterized by a high density of ZrO_2 particles. Large ZrO_2 particles range in size from a few tens of nanometers to several hundred nanometers (Fig. 4a). The configurations of the diffraction maxima in the corresponding diffraction patterns indicate the fulfillment of the Bain relation [21] between the ZrO_2 particles and the vanadium matrix, similar to the previously presented carbide phase. Against the background of large particles, fine ZrO_2 particles ranging in size from 3 to 15 nm are characterized by a predominantly uniform distribution over the volume of the material (Fig. 4b). Microdiffraction patterns from fine particles show ring configurations of weak diffraction maxima (Fig. 4c). As a result of analysis of microdiffraction patterns, it was found that, similarly to the oxidized V–Cr–W–Zr alloy [15], large particles are characterized by the monoclinic (P21/c) modification of ZrO_2 with lattice parameters a = 5,15–5,31 Å; b = 5,21–5,27 Å; c = 5,15–5,38 Å; β = 99,22–99,46° ($Zr_{0.93}O_2$ (P21/c, a = 5.19 Å; b = 5.21 Å; c = 5.38 Å; β = 98.73°) [PDF entry #01-081-1319], $Zr_{0.944}O_2$ (P21/c, a = 5.15 Å; b = 5.20 Å; c = 5.32

Table 1
Oxygen concentrations (C_O) depending on duration (t_O) of oxidation in air (surface scale formation).

t_O, min	90	130	480
C_O, at. %	0.64 ± 0.04	1.02 ± 0.05	1.31 ± 0.06

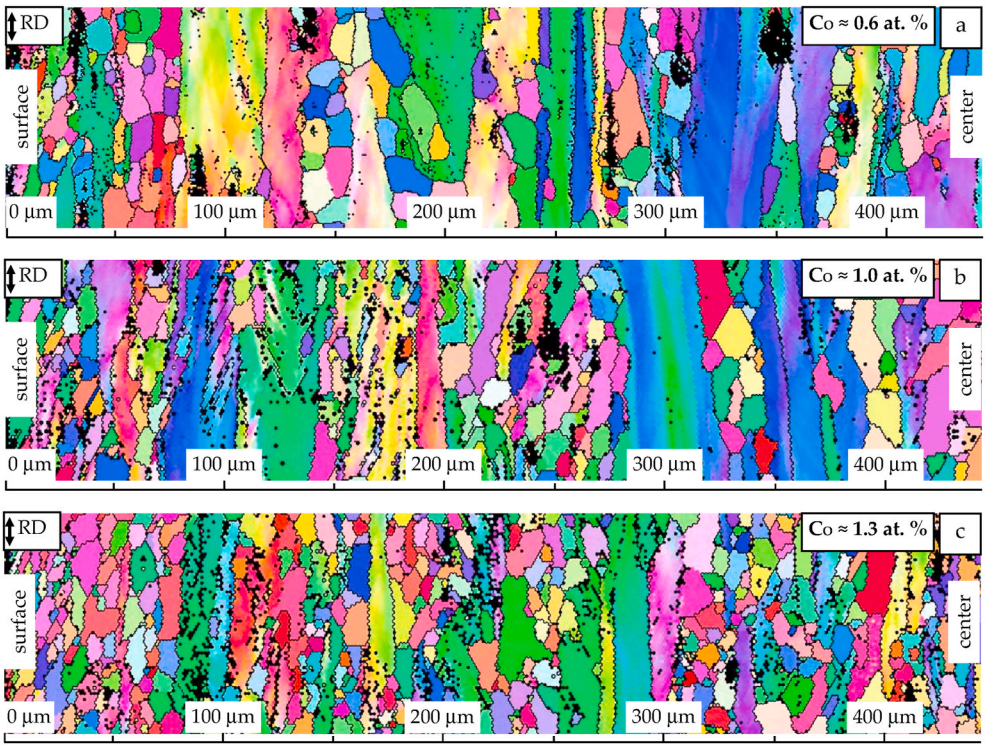

Fig. 3. Grain orientation maps of V–Cr–Zr alloy after CHT with different oxygen concentrations. Stabilizing annealing temperature is 1100 °C. SEM, EBSD.

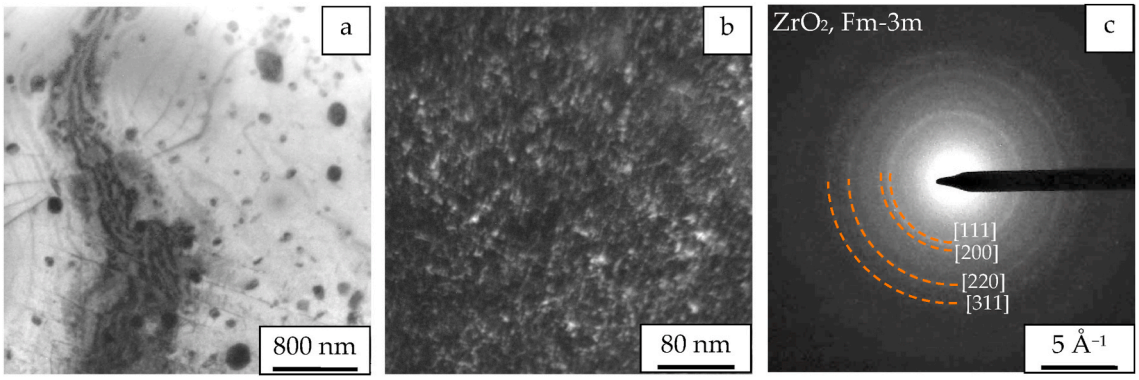

Fig. 4. Structural-phase state of V–Cr–Zr alloy after CHT ($C_O \approx 1.3$ at. %) stabilized at 1100 °C. a – bright-field image of large particles of ZrO_2, b – dark-field image of the dislocation structure and fine-disperse ZrO_2, simultaneously obtained in [110] reflection of the vanadium matrix and [200] of particles. c – microdiffraction pattern from fine particles ZrO_2. TEM.

Å; β = 99.24°) [PDF entry #01-081-1314], ZrO_2 (P21/c, a = 5.14 Å; b = 5.13 Å; c = 5.35 Å; β = 98.88°) [PDF entry #01-080-0966], ZrO_2 (P21/c, a = 5.31 Å; b = 5.21 Å; c = 5.15 Å; β = 99.22°) [PDF entry #00-037-1484]), while fine particles are FCC (Fm-3m) modification of ZrO_2 with the lattice parameter a = 5,1–5,14 Å ($ZrO_{1.87}$ (Fm-3m, a = 5.15 Å) [PDF entry #01-081-1551]), ZrO_2 (Fm-3m, a = 5.14 Å) [PDF entry #01-089-9069]), $ZrO_{2.12}$ (Fm-3m, a = 5.13 Å) [PDF entry #01-081-1550])). The scatter of the lattice parameters near the tabular data is a consequence of minor deviations from the stoichiometric composition.

It has been established that the structural state in the depth of the oxidation front is characterized by a dislocation density of up to (3–5)• 10^{10} cm^{-2}. In addition, the values of the crystal lattice curvature correspond to the maximum values after TMT-II with stabilizing annealing at 1000 °C.

After an hour annealing at 1200 °C, the structural states with different oxygen concentrations (Fig. 5a and b) are generally similar to those formed after an hour annealing at 1100 °C (Fig. 3b and c). At the same time, there are some differences. In particular, at an oxygen concentration of 1 at. % (Fig. 5a) outside the oxidation front, relaxation of the defect state of large anisotropic bands occurs by their fragmentation. This reduces the color gradient. The structural state within the oxidation front (Fig. 5a and b) remains virtually unchanged.

In the course of the dark-field analysis of misorientations, it was found that, even after an hour-long annealing at 1200 °C, high-defect structural states with nonzero values of the components of the bending-torsion tensor remain inside the oxidation front. Fig. 6 shows an example of such an analysis. Dark-field images were obtained in active reflection (−110), forming an angle β ≈ 65.5° with the goniometer tilt axis projection (TAP) (Fig. 6c). At goniometer tilt angle φ = 0°, the extinction contour is excited in subgrain I (Fig. 6a). The subsequent tilt of the goniometer to φ = 1° is accompanied by the division of the contour into two parts ((a) and (b)), which move in opposite directions along the border of subgrains I and II (Fig. 6b). It was found that after

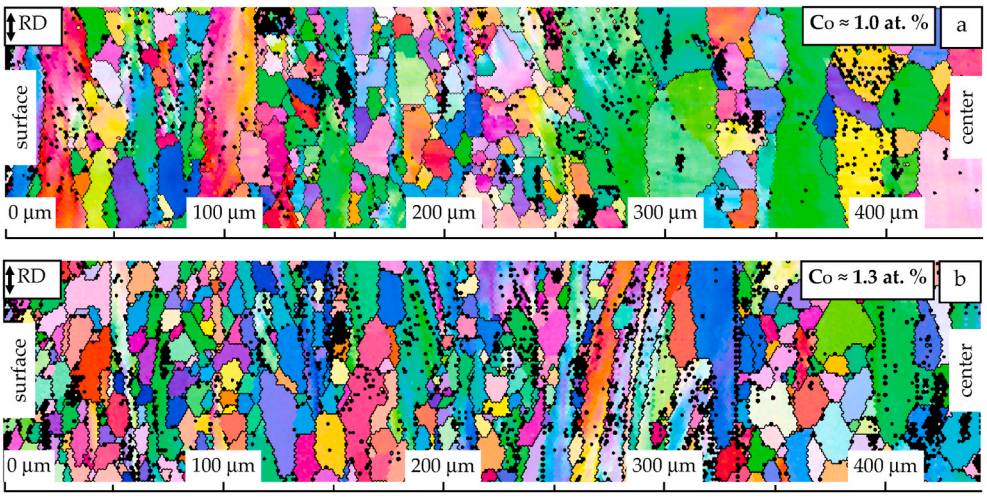

Fig. 5. Grain orientation maps of V–Cr–Zr alloy after CHT with various oxygen concentrations ($C_O \approx 1$ and 1.3 at. %). Stabilizing annealing temperature is 1200 °C. SEM, EBSD.

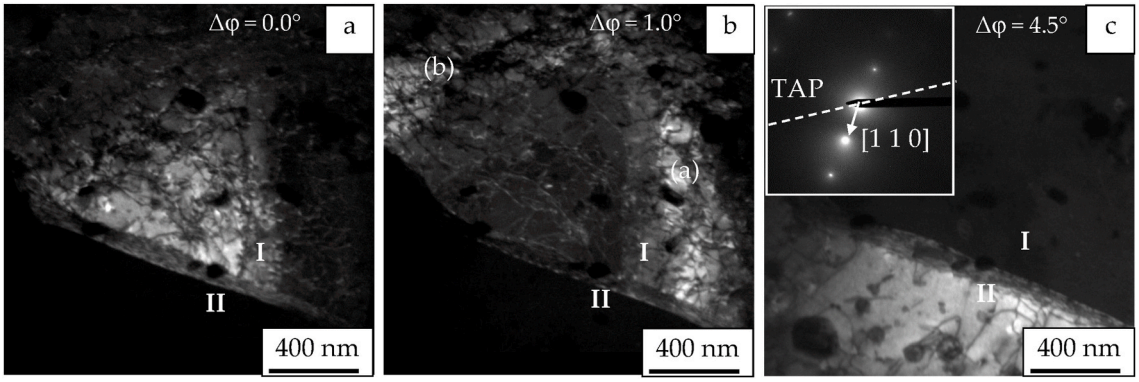

Fig. 6. Dark-field analysis of misorientations in V–Cr–Zr alloy after CHT ($C_O \approx 1.3$ at. %) stabilized at 1200 °C. Images in (−110) reflection at different goniometer tilt angles (φ). TEM.

separation, parts of the contour (a) and (b) move along the boundary at a distance of $\Delta r \approx 200$ nm. In accordance with the formula $\chi_{ij} \approx \Delta\varphi \times \mathrm{Sin}\beta/(\Delta r)$ [18], the value of the component of the bending-torsion tensor χ_{21} reaches 5 deg/μm. At $\varphi = 4.5°$ in the same active reflection in the adjacent subgrain II, the extinction contour is excited almost uniformly (Fig. 6c). This indicates the absence of structural states with crystal lattice curvature in this subgrain. Thus, the boundary between subgrains I and II is a low-angle boundary with a variable orientation vector. In accordance with model concepts [18], such a boundary can be represented as a boundary containing clusters of continuously distributed partial disclinations of the same sign.

The behavior of extinction contours in neighboring subgrains described above indicates that the detected curvature of the crystal lattice is associated with the formation of a high defect structural state and is not a consequence of bending or warping of a thin foil. Thus, the gradient color observed on the grain orientation maps obtained by the

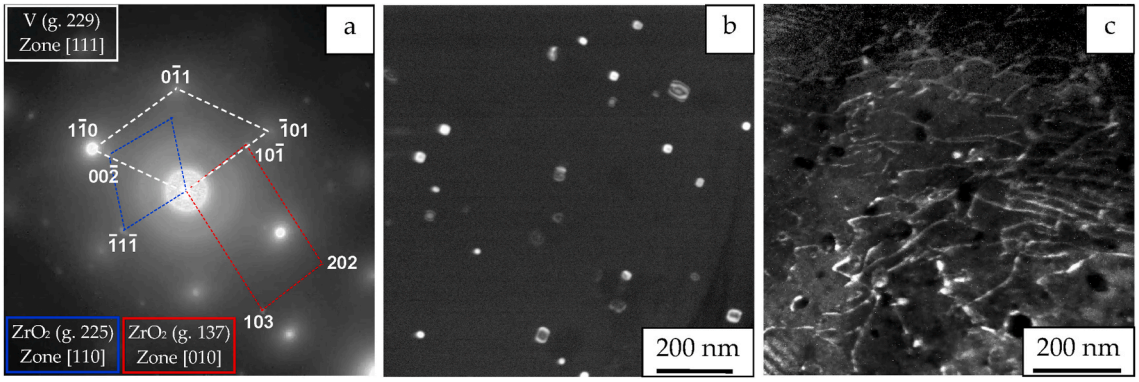

Fig. 7. Microdiffraction pattern (a), dark-field images of the heterophase (b) and dislocation (c) structures of the V–Cr–Zr alloy after CHT with $C_O \approx 1.3$ at. % and annealing at 1200 °C. Image (b) was obtained in reflections of the tetragonal (101) and cubic (111) modifications of ZrO_2; image (c) was obtained in (110) reflection of V. TEM.

EBSD analysis is a consequence of the presence of structural states with a crystal lattice curvature.

A detailed study of the heterophase structure showed that after annealing at 1200 °C (Fig. 7 a) fine (less than 20 nm) ZrO_2 particles still have FCC (Fm-3m) crystal lattice with a slight spread of lattice parameter (a) as well as after annealing at 1100 °C. On their background, larger (20–50 nm in size) ZrO_2 particles were found (Fig. 7a and b), that are characterized by tetragonal (P42/nmc, group 137) modifications of the crystal lattice, the parameters of which vary in the ranges a = 3.49–3.67 Å; c = 4.95–5.32 Å (ZrO_2 (P42/nmc, a = 3.49 Å; c = 4.95 Å) [PDF entry #04-013-4748], ZrO_2 (P42/nmc, a ≈3.60 Å, c ≈ 5.15 Å) [PDF #01-088-1007]), $ZrO_{1.99}$ (P42/nmc, a = 3.61 Å; c = 5.13 Å) [PDF entry #01-080-2155], ZrO_2 (P42/nmc, a = 3.64 Å; c = 5.27 Å) [PDF entry #00-042-1164], ZrO_2 (P42/nmc, a = 3.67 Å; c = 5.32 Å) [PDF entry #04-005-5598], $ZrO_{1.96}$ (P42/nmc, a = 3.62 Å; c = 5.20 Å) [PDF entry #01-081-1546]), as a result of deviations from the stoichiometric composition. Thus, a consequence of an increase in the size of ZrO_2 particles at 1200 °C is the activation of the phase transformation from high-temperature FCC to tetragonal due to a decrease in the relative contribution of surface energy to free energy [24].

After annealing at 1200 °C, the dislocation density decreases to (0.7–3) × 10^{10} cm^{-2}. In particular, in the presented dark-field image (Fig. 7 c), under the indicated diffraction conditions, the dislocation density reaches 1.5 × 10^{10} cm^{-2}. As can be seen, the dislocations are still pinned by nanosized ZrO_2 particles, which indicates the implementation of the dispersion strengthening mechanism, despite the high (0.67 Tm_{elt}) temperature of the stabilizing annealing.

3.2. Microhardness

The propagation of the oxidation front is accompanied by a change in the microhardness values. The microhardness (HV) of the samples before chemical-heat treatment (after TMT-II and 1 h annealing at 1100 °C) is 1.71 ± 0.1 GPa. After CHT with C_O ≈ 0.6 at. % microhardness at a distance of 50 μm from the surface (L) of the sample is HV = 2.03 ± 0.13 GPa (Fig. 8a), which is almost 20 % higher compared to the initial state. At a distance of 100 μm from the surface, HV decreases to 1.8 ± 0.09 GPa, and at distances of more than 150 μm, the microhardness values are close to the initial values.

An increase in the depth of the oxidation front when the oxygen concentration reaches C_O ≈ 1 at. % is accompanied by an increase in microhardness values both near the surface and at a distance from it. At a distance of 50 μm from the surface, HV reaches 2.11 ± 0.1 GPa (Fig. 8a). At distances from 100 to 200 μm, the microhardness decreases from 1.97 to 1.78 GPa. At a distance of more than 200 μm from the surface, HV does not differ from the initial state.

A significant increase in the microhardness in the entire volume of the sample was found when C_O reached 1.3 at. %. At a distance of 50 μm from the surface, its values reach 2.82 ± 0.11 GPa and gradually decrease to 1.95 ± 0.8 GPa at a distance of 450 μm from the surface (Fig. 8a).

An increase in the microhardness of V–Cr–Zr alloy, as a result of an increase in the volume fraction of fine-disperse ZrO_2 particles at high (C_O ≈ 1 and 1.3 at. %) oxygen concentrations, simultaneously occurs at distances comparable to the half-thickness of the sample. In addition, no nanosized ZrC carbides were found in the reaction zone. All this taken together testifies to the implementation of the mechanism of non-equilibrium internal oxidation. Previously, similar effects were found in the process of internal oxidation of zirconium-containing vanadium alloys of other systems [10,15]. It is important to note that since the formation of oxide particles occurs simultaneously throughout the entire thickness of the samples, and the thermodynamic and kinetic conditions of their nucleation and growth are practically independent of the distance from the surface, this ensures a uniform distribution of high dispersion particles over the depth of the reaction zone [10].

Annealing at 1200 °C leads to a decrease in the microhardness of samples after TMT-II and CHT with different oxygen concentrations (Fig. 8b). Samples after TMT-II are characterized by a decrease in microhardness to 1.65 ± 0.10 GPa, which is 4 % decrease compared to annealing at 1100 °C (Fig. 8a).

For samples after CHT with C_O = 1.0 at. %, the HV value near the surface (up to 100 μm) as a result of annealing at 1200 °C decreases to ≈ 1.85 ± 0.1 GPa (Fig. 8b). In this case, at distances of 150–250 μm, HV is 1.75 ± 0.09 GPa. At a distance from the oxidation surface of 300 μm and more, the microhardness corresponds to the TMT-II value with annealing at 1200 °C (Fig. 8b).

In the case of samples after CHT with C_O = 1.3 at. % HV, with an increase in the distance from the surface from 50 μm to 450 μm, decreases from 1.98 ± 0.08 GPa to 1.71 ± 0.07 GPa (Fig. 8b), which corresponds to the microhardness of the samples after TMT-II with annealing at 1100 °C (Fig. 8a).

3.3. Tensile properties

The change in the structural-phase state as a result of TMT, CHT, and stabilizing annealing has a significant effect on the mechanical characteristics (yield strength ($\sigma_{0.1}$) and relative elongation (δ)) of V–Cr–Zr alloy at room and elevated temperatures. Fig. 9 shows σ-ε curves of specimen tension at different temperatures (T_t) depending on processing conditions.

Table 2 shows the values of yield strength ($\sigma_{0.1}$) and relative elongation (δ) depending on the test temperature of V–Cr–Zr alloy after TMT-II with stabilizing annealing at 1000 and 1100 °C. As can be seen from this table, an increase in the stabilization temperature leads to a decrease in the yield strength at room temperature by almost 12 %, and at 800 °C by 14 %. After an increase in the stabilizing annealing

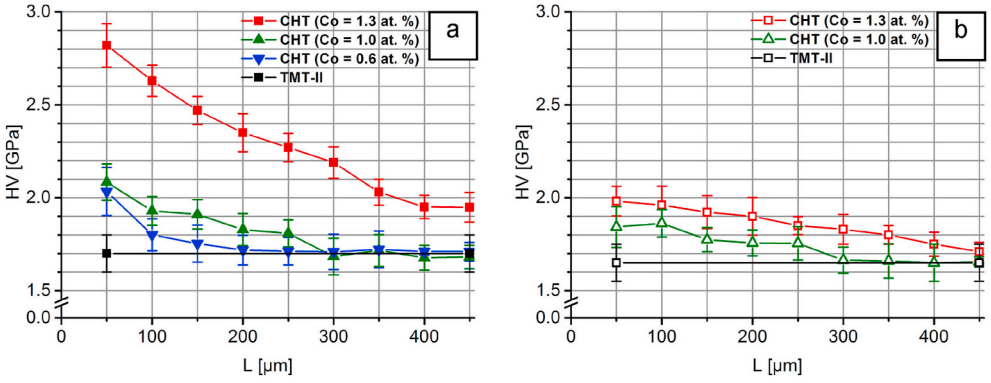

Fig. 8. Microhardness (HV) of V–Cr–Zr alloy after different processing conditions depending on the distance from the surface (L). a – stabilizing annealing temperature 1100 °C. b – stabilizing annealing temperature 1200 °C.

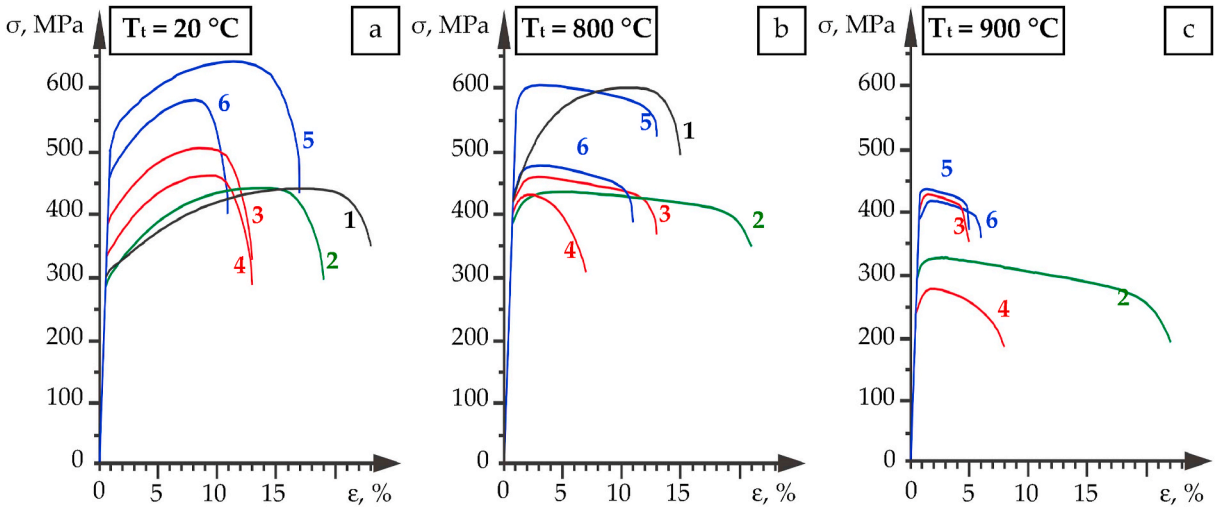

Fig. 9. Tension σ-ε curves for V–Cr–Zr alloy after TMT-II (1) and CHT with different oxygen concentrations: $C_O \approx 0.6$ at. % (2); $C_O \approx 1.0$ at. % (3,4); $C_O \approx 1.3$ at. % (5,6). 1,2,3,5 – after stabilizing annealing at 1100 °C. 4,6 – after stabilizing annealing at 1200 °C. a – $T_t = 20$ °C; b – $T_t = 800$ °C; c – $T_t = 900$ °C.

Table 2
Yield strength ($\sigma_{0.1}$) and relative elongation (δ) of V–Cr–Zr alloy after TMT-II with stabilizing annealing at 1000 and 1100 °C.

T, °C	T_t = **20 °C**		T_t = **800 °C**		T_t = **900 °C**	
	$\sigma_{0.1}$, MPa	δ, %	$\sigma_{0.1}$, MPa	δ, %	$\sigma_{0.1}$, MPa	δ, %
1000	344 ± 17	21 ± 6	245 ± 12	8 ± 3	173 ± 11	21 ± 10
1100	304 ± 15	24 ± 6	211 ± 11	15 ± 5	–	–

temperature, the ductility of the alloy at room temperature remains almost unchanged, while at an elevated temperature it almost doubles (Table 2).

After TMT-II with stabilization at 1000 °C under tensile conditions at 900 °C (Table 2), the values of the yield strength of V–Cr–Zr alloy are comparable to the values of the yield strength of the alloys of the V–4Ti–4Cr system at 800 °C after such stabilization [25–27].

The values of the yield strength ($\sigma_{0.1}$) and relative elongation (δ) depending on the test temperature of V–Cr–Zr alloy after different CHT modes with stabilizing annealing at 1100 °C are given in Table 3.

In the case of $C_O \approx 0.6$ at. % the yield strength of V–Cr–Zr alloy at room test temperature is comparable to the values after TMT-II stabilized at 1100 °C. However, at a test temperature of 800 °C, the yield strength of the alloy after this CHT regime is 14 % lower than the values after TMT. Moreover, under tensile conditions at 900 °C, the yield strength decreases dramatically by almost 20 % compared to 800 °C. At all tension temperatures, V–Cr–Zr alloy after CHT ($C_O \approx 0.6$ at. %) exhibits a plasticity of 20 %.

An increase in C_O from 0.6 to 1 at. % (Table 3) leads to an increase in the yield strength at all studied tensile temperatures: at 20 °C $\sigma_{0.1}$ increases by ≈ 30 %; at 800 °C – by ≈ 20 %; at 900 °C – by ≈ 35 %. The indicated increase in the yield strength with an increase in oxygen concentration is accompanied by a more than one and a half-fold decrease in plasticity at 20 °C and 800 °C, while at 900 °C it decreases by 4.6 times. In comparison with TMT-II with stabilization at 1100 °C, the increase in the yield strength at 20 °C and 800 °C is ≈ 25 % and ≈ 4 %, respectively. At 900 °C, the yield strength corresponds to the values typical for alloys of the V–4Ti–4Cr system at 800 °C [25–27]. This indicates at least a 100 °C increase in the thermal stability of the strength properties of V–Cr–Zr alloy in comparison with the alloys of the V–4Ti–4Cr system.

Upon reaching $C_O \approx 1.3$ at. % material is characterized by the maximum values of the yield strength (Table 3). Compared to $C_O \approx 0.6$ at. % increase in $\sigma_{0.1}$ values at room temperature is ≈ 75 %, and at elevated temperatures (800 and 900 °C) by 43 and 50 %, respectively. Plasticity does not change at elevated temperatures, and even increases by 1.3 times at room temperature.

The values of the yield strength and plasticity at different tension temperatures in the case of stabilization annealing at 1200 °C are presented in Table 4.

Under tension conditions at room temperature specimens with $C_O \approx 1$ and 1.3 at. % are characterized by more than 10 % decrease in yield strength compared to stabilization at 1100 °C. At a tension temperature of 800 °C, a decrease in the yield strength for $C_O \approx 1$ and 1.3 at. % is 10 % and 15 %, respectively. The largest decrease of $\sigma_{0.1}$, about 30 %, is observed in the case of tension at 900 °C of specimens with $C_O \approx 1$ at. %. At the same tensile temperature, samples with $C_O \approx 1.3$ at. % show a decrease in yield strength of less than 10 %. Note that after stabilization at 1200 °C, the plasticity remains almost unchanged. Only in the case of tension at 800 °C for specimens with $C_O \approx 1$ at. % its one and a half times decrease is observed.

4. Discussion

A distinctive feature of CHT is an increase in oxygen concentration, which contributes to an increase in the volume fraction of the second phase. The estimate showed that at $C_O \approx 0.64$ at. %, $C_O \approx 1.02$ at. %, $C_O \approx 1.31$ at. % volume fraction (f) of the second phase based on ZrO_2 in the V–Cr–Zr alloy is 0.79 %, 1.25 %, 1.61 %, respectively. These values are

Table 3
Yield strength ($\sigma_{0.1}$) and relative elongation (δ) of V–Cr–Zr alloy after CHT. Stabilizing annealing temperature 1100°C

C_O, at. %	T_t = **20 °C**		T_t = **800 °C**		T_t = **900 °C**	
	$\sigma_{0.1}$, MPa	δ, %	$\sigma_{0.1}$, MPa	δ, %	$\sigma_{0.1}$, MPa	δ, %
0.6	291 ± 15	19 ± 5	181 ± 9	21 ± 5	148 ± 8	23 ± 12
1.0	379 ± 19	13 ± 7	219 ± 11	13 ± 6	200 ± 10	5 ± 2
1.3	505 ± 25	17 ± 6	273 ± 12	13 ± 5	212 ± 11	5 ± 3

Table 4
Yield strength ($\sigma_{0.1}$) and relative elongation (δ) of V–Cr–Zr alloy after CHT. Stabilizing annealing temperature 1200°C

C_O, at. %	T_t = **20 °C**		T_t = **800 °C**		T_t = **900 °C**	
	$\sigma_{0.1}$, MPa	δ, %	$\sigma_{0.1}$, MPa	δ, %	$\sigma_{0.1}$, MPa	δ, %
1.0	336 ± 17	13 ± 6	200 ± 10	7 ± 4	141 ± 19	8 ± 2
1.3	452 ± 25	13 ± 5	233 ± 12	11 ± 5	194 ± 18	6 ± 3

significantly (an order of magnitude or more) higher compared to carbide strengthening in which the volume fraction of the second phase (f ≈ 0.08 %) based on ZrC in this alloy is limited by the carbon concentration (0.042 at. %). Unlike CHT, in the TMT process of vanadium alloys, only carbon redistribution is possible during the transformation of metastable vanadium-based carbides into stable zirconium-based or titanium-based carbides [8,13]. Moreover, due to the low solubility of carbon in vanadium [6], there are currently no effective methods for further increasing its concentration in such alloys after their melting. As a result, it is not possible to increase the volume fraction of the ZrC-based carbide phase in the alloy after smelting to values commensurate with the ZrO_2-based oxide phase, and it is not possible to obtain such strengthening effects. At the same time, it was shown in Ref. [28] that the yield strength of carbide-strengthened alloy V-1.34Zr-0.13O-0.04N-1.06C (at. %), in which there was initially high (f ≈ 1.99 %) volume fraction of the second phase based on ZrC, after a similar treatment (TMT-II with stabilization at 1000 °C) under tension conditions at 800 °C can reach even higher values.

Table 5 shows estimates of the effects of dispersion strengthening (the values of Orowan stress (Δσ)) depending on the volume fraction (*f*) and the size (R_p – radius) of the particles of the second phases. We used the ratio $\Delta\sigma \approx Gb/\lambda$ [23], where $\lambda \approx R_p \bullet (2\pi)^{1/2} \bullet (3f)^{-1/2}$ is the distance between particles (for vanadium, the shear modulus G ≈ 47,300 MPa [29], and the modulus of the Burgers vector of gliding dislocations b = a/2 <111> [29] ≈ 0.262 nm).

It should be noted that dispersion strengthening by the Orowan mechanism [23] is extremely sensitive to the size of particles that pin the dislocation structure. Estimates, assuming that the entire volume fraction of the second phase is present in the form of fine particles providing dispersion strengthening, demonstrate a high level of Orowan stresses (Table 5). At the same time, the efficiency of dispersion strengthening decreases in proportion to the increase in the size (diameter) of the particles. In particular, an increase in the particle size from 3 nm to 15 nm, with a constant volume fraction, leads to a fivefold decrease in the Orowan stress. In addition to fine-disperse particles, the material exhibits a high density of large particles ranging in size from several tens to several hundred nm, which practically do not participate in dispersion strengthening. With a small amount and low density, it is the large particles that can account for a significant volume fraction of the entire second phase. For comparison, a particle with a diameter of 100 nm has a volume of $5.2 \bullet 10^5$ nm^3, which is almost 1000 times larger than the volume of particle with a size (diameter) of 10 nm (523 nm^3) and almost 37,000 times larger than the volume of a particle with a size of 3 nm (14.13 nm^3). In addition, it is extremely difficult to assess the direct contribution from fine particles of one size or another.

Comparison of the strength of the alloy after TMT and CHT with stabilization at 1100 °C allows demonstrating the effect of the volume fraction of the second phase. In the case of C_O = 1.0 at. %, the average $\sigma_{0.1}$ values are higher compared to TMT-II by 75 MPa at T_t = 20 °C and by 8 MPa at T_t = 800 °C. At a higher concentration of C_O = 1.3 at. % increase in $\sigma_{0.1}$, in comparison with TMT-II, at T_t = 20 °C and T_t = 800 °C is 225 and 89 MPa, respectively. Such an increase in mechanical properties at room and elevated temperatures, in our opinion, is mainly due to dispersion strengthening. As is known [30–32], the efficiency of solid solution strengthening by introduction elements of alloys based on refractory metals dramatically decreases at temperatures above 0.45 T_{melt}. In many respects, this concerns carbide-strengthened alloys. In this case, an important distinguishing feature of oxygen from carbon is its high solubility in vanadium at elevated temperatures [6]. In Refs. [10,15], we showed that in the CHT process, by the mechanism of nonequilibrium internal oxidation in vanadium alloys, not only a high density of fine particles based on ZrO_2 is formed, but also a high oxygen concentration in the solid solution is achieved, which is one of the main factors determining an increase in the thermal stability of such alloys. That is, when the growth of particles is controlled by the diffusion of zirconium atoms, an increase in the concentration of oxygen in the solid solution leads to a decrease in the rate of coagulation of oxides and an increase in the thermal stability of the high-disperse heterophase state [10,15].

In our opinion, it is the high density of fine particles based on ZrO_2, along with an increased oxygen concentration in the solid solution (up to 0.1 at. %), that contribute to the retention of high-defect structural states with nonzero values of the crystal lattice curvature even after high-temperature (0.67 T_{melt}) anneals. In particular, these are the structural states with crystal lattice curvature (χ_{ij}) up to 5 deg/μm found after annealing at 1200 °C. As is known [18], strong interdislocation interactions and high local internal stresses characteristic of these structural states make it difficult to analyze these states within the framework of the traditional dislocation theory of plasticity and require taking into account collective phenomena in ensembles of strongly interacting dislocations of the same sign. Within the framework of concepts [33], such structural states can be represented as clusters of geometrically necessary dislocations of the same sign ($\rho_{\pm}$). The estimates made according to the formula $\rho_{\pm} = \rho_- - \rho_+ = \chi_{ij}/|b|$ [18] (where |b| for the Burgers dislocation vector modulus in vanadium equal to 0.3024 nm) show that the formation of a crystal lattice curvature of 5 deg/μm in vanadium requires a density of geometrically necessary dislocations of the same sign ≈ $3\ 10^{10}$ cm^{-2}. As can be seen, this value coincides with the lower boundary of the range of the observed scalar dislocation density in the depth of the oxidation front after stabilization at 1100 °C and is 3 times higher than the maximum values of the scalar dislocation density after TMT II with stabilization at 1100 °C. According to Ref. [18], structural states with a crystal lattice curvature are characterized by the presence of local internal stresses (σ_{loc}). Estimates made using the formula $\sigma_{loc} \approx \chi_{ij} E \Delta h/2$ [18] (where E is Young's modulus of pure vanadium, 123 GPa; Δh is the characteristic size of the curvature zone, 200 nm) show that σ_{loc} reaches the values of E/115, which corresponds to elastic deformation of the crystal lattice $\varepsilon = \Delta d/d \approx 0{,}00873$ (less than 1 %). With an increase in the size of the zone of the crystal lattice curvature of 5 deg/μm to 400 nm, σ_{loc} increases to E/57, therefore, ε increases to 0.01746, that is, it is more than 1.5 %.

As is known [34–36], the formation of high defect structural states, including nanocrystalline and submicrocrystalline, in many metals and alloys is often accompanied by a decrease in the recrystallization temperature, reaching several hundred degrees, which has a significant effect on the complex of their physical and mechanical properties. In the case of heterophase alloys, which include low-activation vanadium alloys of different systems, the thermal stability of high defect structural states is determined by the volume fraction of fine particles in combination with the concentration of interstitial impurities in the solid solution. In particular, it was shown in Ref. [37] that the alloy V-4.47Ti-4.26Cr-0.063O-0.040N-0.055C (at. %), characterized by a volume fraction of fine TiC particles no more than 0.08 %, has a high defect nanostructural state and corresponding high values of microhardness retained only up to a temperature of 600 °C (0.4 T_{melt}). In this case, the volume fraction of the entire oxycarbonitride phase of the Ti

Table 5
Estimates of Orowan stresses (Δσ, MPa) depending on the volume fraction and particle size of the second phase.

Particles volume fraction, *f*, %	Particles size (diameter – $2 \bullet R_p$), nm			
	3	5	10	15
	Orowan stresses Δσ, MPa			
1.61	724	435	217	145
1.25	638	383	191	128
1.00	571	343	171	114
0.79	507	304	152	101
0.11	189	114	57	38
0.08	161	97	48	32
0.04	114	69	34	23
0.02	81	48	24	16

(N, C, O) type based on Ti, as the most active phase-forming element, according to estimates [8], does not exceed 0.24 %. After annealing at 800 °C (0.5 T_{melt}), a dramatic decrease in the microhardness values and activation of recrystallization processes were found.

At the same time, in the internally oxidized V–Cr–Zr alloy with a high (1.3 at. %) oxygen concentration studied in this work, in paper [16] authors demonstrated a significant (up to 800 °C, ~ 0.5 T_{melt}) increase in the thermal stability of high-defect structural states formed under conditions of high plastic deformations. Also an increase in the Hall-Petch coefficient by 60 %, compared to pure vanadium, was found. In this case, the fine-crystalline state is retained even after annealing at a temperature of 1200 °C, which is 0.67 T_{melt}.

The presence of a high density of fine particles along with a high concentration of oxygen in the solid solution promotes blocking of dislocation slip, thereby ensuring the stability of the defect and grain structure even at high temperatures. This fact testifies to the high efficiency of dispersion and substructural strengthening. In this regard, the use of CHT methods based on internal oxidation as a way to increase the volume fraction of fine particles and the oxygen concentration in a solid solution compares favorably with carbide strengthening when creating high-defect structural states with increased thermal stability and level of strength properties.

5. Conclusions

A comparative study has shown that the implementation of CHT by the method of low-temperature diffusion alloying provides a significant increase in the thermal stability of the microstructure and properties of V–Cr–Zr alloy compared to the increase in the efficiency of carbide strengthening as a result of using TMT. Samples after CHT demonstrate comparable or significantly higher values of yield strength compared to TMT, including after stabilizing anneals at higher temperatures.

The effectiveness of this approach is associated not only with the possibility of a controlled increase in the volume fraction of ZrO_2-based fine particles, but also with an increase in the oxygen concentration in the solid solution, which leads to a decrease in the rate of coagulation of oxides and an increase in the thermal stability of the high disperse heterophase state. The latter manifests itself in the retention of high-defect structural states with nonzero values of the crystal lattice curvature even after high-temperature (0.67 T_{melt}) anneals.

The high efficiency of dispersion and substructural strengthening is a consequence of blocking dislocation slip by fine particles stabilized by oxygen in a solid solution, which ensures the stability of a high-defect state even at high temperatures.

Funding

The work was performed according to the Government research assignment for ISPMS SB RAS, project FWRW-2021-0008.

Data availability

The data are available on request.

CRediT authorship contribution statement

Ivan A. Ditenberg: Conceptualization, Data curation, Writing, Supervision. **Ivan V. Smirnov:** Data curation, Investigation, and. **Konstantin V. Grinyaev:** Investigation, Writing, and. **Alexander N. Tyumentsev:** Conceptualization, Data curation, and. **Vyacheslav M. Chernov:** Conceptualization. **Mikhail M. Potapenko:** Investigation, Writing.

Declaration of competing interest

The authors declare that they have no known competing financial interests or personal relationships that could have appeared to influence the work reported in this paper.

Acknowledgment

The investigation has been performed using the equipment of the Tomsk Materials Center for Shared Use of Scientific Equipment at National Research Tomsk State University.

References

[1] T. Muroga, T. Nagasaka, K. Abe, V.M. Chernov, H. Matsui, D.L. Smith, Z.Y. Xu, S. J. Zinkle, Vanadium alloys - overview and recent results, J. Nucl. Mater. (2002) 307–311, https://doi.org/10.1016/S0022-3115(02)01253-9, 547–554.
[2] T. Muroga, J.M. Chen, V.M. Chernov, R.J. Kurtz, M. Le Flem, Present status of vanadium alloys for fusion applications, J. Nucl. Mater. 455 (2014) 263–268, https://doi.org/10.1016/j.jnucmat.2014.06.025.
[3] R.J. Kurtz, K. Abe, V.M. Chernov, D.T. Hoelzer, H. Matsui, T. Muroga, G.R. Odette, Recent progress on development of vanadium alloys for fusion, J. Nucl. Mater. (2004) 329–333, https://doi.org/10.1016/j.jnucmat.2004.04.299, 47–55.
[4] S.J. Zinkle, A. Möslang, T. Muroga, H. Tanigawa, Multimodal options for materials research to advance the basis for fusion energy in the ITER era, Nucl. Fusion 53 (2013) 104024, https://doi.org/10.1088/0029-5515/53/10/104024.
[5] V.V. Shyrokov, C.B. Vasyliv, O.V. Shyrokov, Ways of improving the high-temperature work service of vanadium and some alloys used in reactors, J. Nucl. Mater. 394 (2009) 114–122, https://doi.org/10.1016/j.jnucmat.2009.07.009.
[6] E.G.E. Fromm, Gasses and Carbon in Metals, Springer Verlag, Berlin, 1976.
[7] S. Oda, H. Kurishita, Y. Tsuruoka, S. Kobayashi, K. Nakai, H. Matsui, High temperature strength of fine-grained, particle-dispersed V–(1.7–2.4)wt%Y alloys with different grain sizes and particle densities, J. Nucl. Mater. (2004) 329–333, https://doi.org/10.1016/j.jnucmat.2004.04.308, 462–466.
[8] A.N. Tyumentsev, A.D. Korotaev, Y.P. Pinzhin, I.A. Ditenberg, S.V. Litovchenko, Y. V. Shuba, N.V. Shevchenko, V.A. Drobishev, M.M. Potapenko, V.M. Chernov, Effect of the modes of thermomechanical treatment on the formation of the multiphase and grain structure of V–4Ti–4Cr alloys, J. Nucl. Mater. (2004) 329–333, https://doi.org/10.1016/j.jnucmat.2004.04.074, 429–433.
[9] H. Kurishita, S. Oda, S. Kobayashi, K. Nakai, T. Kuwabara, M. Hasegawa, H. Matsui, Effect of 2wt% Ti addition on high-temperature strength of fine-grained, particle dispersed V–Y alloys, J. Nucl. Mater. (2007) 367–370, https://doi.org/10.1016/j.jnucmat.2007.03.071, 848–852.
[10] A.N. Tyumentsev, A.D. Korotaev, Y.P. Pinzhin, S.V. Ovchinnikov, I.A. Ditenberg, A. K. Shikov, M.M. Potapenko, V.M. Chernov, Effect of internal oxidation on the microstructure and mechanical properties of vanadium alloys, J. Nucl. Mater. (2007) 367–370, https://doi.org/10.1016/j.jnucmat.2007.03.070, 853–857.
[11] T. Sakamoto, H. Kurishita, S. Kobayashi, K. Nakai, H. Arakawa, H. Matsui, High temperature deformation of a fine-grained and particle-dispersed V-2.3%Y-4%Ti-3%Mo alloy, Mater. Trans. 47 (2006) 2497–2503, https://doi.org/10.2320/matertrans.47.2497.
[12] T. Sakamoto, H. Kurishita, S. Kobayashi, K. Nakai, High temperature deformation of V-1.6Y-8.5W-(0.08, 0.15)C alloys, J. Nucl. Mater. (2009) 386–388, https://doi.org/10.1016/j.jnucmat.2008.12.187, 602–605.
[13] A.N. Tyumentsev, I.A. Ditenberg, K.V. Grinyaev, I.V. Smirnov, Y.P. Pinzhin, V. M. Chernov, M.M. Potapenko, V.A. Drobyshev, M.V. Kravtsova, The effect of thermomechanical treatment regimes on microstructure and mechanical properties of V–Me(Cr, W)–Zr–C alloys, Phys. At. Nucl. 78 (2015) 1092–1099, https://doi.org/10.1134/S1063778815100130.
[14] V.M. Chernov, M.M. Potapenko, V.A. Drobyshev, M.V. Kravtsova, A. N. Tyumentsev, S.V. Ovchinnikov, I.A. Ditenberg, Y.P. Pinzhin, A.D. Korotaev, I. V. Smirnov, K.V. Grinyaev, I.I. Sukhanov, Microstructure and mechanical properties of V–Me(Cr,W)–Zr alloys as a function of their chemical–thermal treatment modes, Nucl. Mater. Energy. 3–4 (2015) 17–21, https://doi.org/10.1016/j.nme.2015.04.001.
[15] I.A. Ditenberg, I.V. Smirnov, K.V. Grinyaev, A.N. Tyumentsev, Influence of oxygen concentration on the formation features and thermal stability of the V–Cr–W–Zr alloy microstructure under combined treatment conditions, Mater. Char. 168 (2020) 110517, https://doi.org/10.1016/j.matchar.2020.110517.
[16] I.A. Ditenberg, A.N. Tyumentsev, I.V. Smirnov, K.V. Grinyaev, V.M. Chernov, Thermal stability of nanostructured internally oxidized vanadium alloy with combined dispersion and substructural hardening, Phys. Mesomech. 22 (2019) 496–503, https://doi.org/10.1134/S1029959919060067.
[17] A.J. Schwartz, M. Kumar, B.L. Adams, D.P. Field (Eds.), Electron Backscatter Diffraction in Materials Science, Springer US, Boston, MA, 2009, https://doi.org/10.1007/978-0-387-88136-2.
[18] A.N. Tyumentsev, I.A. Ditenberg, A.D. Korotaev, K.I. Denisov, Lattice curvature evolution in metal materials on meso- and nanostructural scales of plastic deformation, Phys. Mesomech. 16 (2013) 319–334, https://doi.org/10.1134/S1029959913040061.
[19] J.D. Eshelby, The continuum theory of lattice defects, Solid State Phys. 3 (1956) 79–144, https://doi.org/10.1016/S0081-1947(08)60132-0.
[20] R. de Wit, Linear theory of static disclinations, in: J.A. Simmons, R. de Wit (Eds.), Fundamental Aspects of Dislocation vol. 2, National Bureau of Standards, USA, Houston, 1970, pp. 651–673.

[21] K.H. Lo, C.H. Shek, J.K.L. Lai, Recent developments in stainless steels, Mater. Sci. Eng. R Rep. 65 (2009) 39–104, https://doi.org/10.1016/j.mser.2009.03.001.
[22] P.B. Hirsch, A. Howie, R.B. Nicholson, D.W. Pashley, M.J. Whelan, Electron Microscopy of Thin Crystals, Butterworths, London, Great Britain, 1965.
[23] J.W. Martin, Michromechanisms in Particle-Hardened Alloys, Cambridge University Press, Cambridge, 1980.
[24] I.D. Morokhov, V.I. Petinov, L.I. Trusov, V.F. Petrunin, Structure and properties of fine metallic particles, Sov. Phys. Usp. 24 (4) (1981) 295–317, https://doi.org/10.1070/PU1981v024n04ABEH004800.
[25] J.M. Chen, V.M. Chernov, R.J. Kurtz, T. Muroga, Overview of the vanadium alloy researches for fusion reactors, J. Nucl. Mater. 417 (2011) 289–294, https://doi.org/10.1016/j.jnucmat.2011.02.015.
[26] T.S. Bray, H. Tsai, L.J. Nowicki, M.C. Billone, D.L. Smith, W.R. Johnson, P. W. Trester, Tensile and impact properties of V-4Cr-4Ti alloy heats 832665 and 832864, J. Nucl. Mater. 283–287 (2000) 633–636, https://doi.org/10.1016/S0022-3115(00)00229-4.
[27] J.M. Chen, T. Nagasaka, T. Muroga, S.Y. Qiu, C. Li, N. Nita, Mechanical properties of V–4Cr–4Ti strengthened by precipitation and cold rolling, J. Nucl. Mater. 374 (2008) 298–303, https://doi.org/10.1016/j.jnucmat.2007.08.012.
[28] I.A. Ditenberg, A.N. Tyumentsev, K.V. Grinyaev, V.M. Chernov, M.M. Potapenko, V.A. Drobyshev, Features of the microstructure and mechanical properties of V-Zr-C alloy depending on modes of thermomechanical treatment, Inorg. Mater. Appl. Res. 4 (2013) 438–443, https://doi.org/10.1134/S2075113313050055.
[29] J.P. Hirth, J. Lothe, T. Mura, Theory of Dislocations, second ed., Krieger Publishing Company, Malabar, Florida, 1982.
[30] I. Machlin, R.T. Begley, E.D. Weisert (Eds.), Refractory Metal Alloys Metallurgy and Technology, Plenum Press, New York, 1968, https://doi.org/10.1007/978-1-4684-9120-3.
[31] T.E. Tietz, J.W. Wilson, Behavior and Properties of Refractory Metals, Stanford University Press, Stanford California, 1965.
[32] E.J. Delgrosso, C.E. Carlson, J.J. Kaminsky, Development of niobium-zirconium-carbon alloys, J. Less Common. Met. 12 (1967) 173–201, https://doi.org/10.1016/0022-5088(67)90114-2.
[33] M.F. Ashby, The deformation of plastically non-homogeneous materials, Philos. Mag. A J. Theor. Exp. Appl. Phys. 21 (1970) 399–424, https://doi.org/10.1080/14786437008238426.
[34] R.Z. Valiev, R.K. Islamgaliev, I.V. Alexandrov, Bulk nanostructured materials from severe plastic deformation, Prog. Mater. Sci. 45 (2000) 103–189, https://doi.org/10.1016/S0079-6425(99)00007-9.
[35] J. Lian, R.Z. Valiev, B. Baudelet, On the enhanced grain growth in ultrafine grained metals, Acta Metall. Mater. 43 (1995) 4165–4170, https://doi.org/10.1016/0956-7151(95)00087-C.
[36] H. Gleiter, Nanocrystalline materials, Prog. Mater. Sci. 33 (1989) 223–315, https://doi.org/10.1016/0079-6425(89)90001-7.
[37] I.A. Ditenberg, A.N. Tyumentsev, Thermal stability of microstructure and microhardness of heterophase BCC-alloys after torsional deformation on Bridgman Anvils, Russ. Phys. J. 60 (2018) 1993–1999, https://doi.org/10.1007/s11182-018-1313-x.